

## Regular Article

## LYMPHOID NEOPLASIA

## Diffuse large B-cell lymphoma patient-derived xenograft models capture the molecular and biological heterogeneity of the disease

Bjoern Chapuy,<sup>1,\*</sup> Hongwei Cheng,<sup>2,\*</sup> Akira Watahiki,<sup>2</sup> Matthew D. Ducar,<sup>3</sup> Yuxiang Tan,<sup>4</sup> Linfeng Chen,<sup>1</sup> Margaretha G. M. Roemer,<sup>1</sup> Jing Ouyang,<sup>1</sup> Amanda L. Christie,<sup>1</sup> Liye Zhang,<sup>4</sup> Daniel Gusenleitner,<sup>4</sup> Ryan P. Abo,<sup>3</sup> Pedro Farinha,<sup>5</sup> Frederike von Bonin,<sup>6</sup> Aaron R. Thorner,<sup>3</sup> Heather H. Sun,<sup>7</sup> Randy D. Gascoyne,<sup>5</sup> Geraldine S. Pinkus,<sup>7</sup> Paul van Hummelen,<sup>3</sup> Gerald G. Wulf,<sup>6</sup> Jon C. Aster,<sup>7</sup> David M. Weinstock,<sup>1</sup> Stefano Monti,<sup>4</sup> Scott J. Rodig,<sup>7</sup> Yuzhuo Wang,<sup>2,†</sup> and Margaret A. Shipp<sup>1,†</sup>

<sup>1</sup>Department of Medical Oncology, Dana-Farber Cancer Institute, Boston, MA; <sup>2</sup>Experimental Therapeutics, British Columbia Cancer Agency, Vancouver, BC, Canada; <sup>3</sup>Center for Cancer Genome Discovery, Dana-Farber Cancer Institute, Boston, MA; <sup>4</sup>Section of Computational Biomedicine, Boston University School of Medicine, Boston, MA; <sup>5</sup>Department of Pathology and Laboratory Medicine and the Center for Lymphoid Cancer, British Columbia Cancer Agency, Vancouver, BC, Canada; <sup>6</sup>Department of Hematology and Oncology, Georg-August University Goettingen, Goettingen, Germany; and <sup>7</sup>Department of Pathology, Brigham and Women's Hospital, Boston, MA

## Key Points

- Our generated PDX models reflect the immunophenotypic, transcriptional, genetic, and functional heterogeneity of primary DLBCL.
- The experimental and analytical approach will inform the development of additional PDX models and facilitate preclinical drug discovery.

Diffuse large B-cell lymphoma (DLBCL) is a heterogeneous disease defined by transcriptional classifications, specific signaling and survival pathways, and multiple low-frequency genetic alterations. Preclinical model systems that capture the genetic and functional heterogeneity of DLBCL are urgently needed. Here, we generated and characterized a panel of large B-cell lymphoma (LBCL) patient-derived xenograft (PDX) models, including 8 that reflect the immunophenotypic, transcriptional, genetic, and functional heterogeneity of primary DLBCL and 1 that is a plasmablastic lymphoma. All LBCL PDX models were subjected to whole-transcriptome sequencing to classify cell of origin and consensus clustering classification (CCC) subtypes. Mutations and chromosomal rearrangements were evaluated by whole-exome sequencing with an extended bait set. Six of the 8 DLBCL models were activated B-cell (ABC)-type tumors that exhibited ABC-associated mutations such as *MYD88*, *CD79B*, *CARD11*, and *PIM1*. The remaining 2 DLBCL models were germinal B-cell type, with characteristic alterations of *GNA13*, *CREBBP*, and *EZH2*, and chromosomal translocations involving *IgH* and either *BCL2* or *MYC*. Only 25% of the DLBCL PDX models harbored inactivating *TP53* mutations, whereas

75% exhibited copy number alterations of *TP53* or its upstream modifier, *CDKN2A*, consistent with the reported incidence and type of *p53* pathway alterations in primary DLBCL. By CCC criteria, 6 of 8 DLBCL PDX models were B-cell receptor (BCR)-type tumors that exhibited selective surface immunoglobulin expression and sensitivity to entospletinib, a recently developed spleen tyrosine kinase inhibitor. In summary, we have established and characterized faithful PDX models of DLBCL and demonstrated their usefulness in functional analyses of proximal BCR pathway inhibition. (*Blood*. 2016;127(18):2203-2213)

## Introduction

Diffuse large B-cell lymphoma (DLBCL) is the most common non-Hodgkin lymphoma in adults, accounting for ~40% of B-cell malignancies. DLBCL is a clinically and genetically heterogeneous disease with recognized subtypes based on morphology, transcriptional profiles, and multiple low-frequency genetic alterations including chromosomal translocations, somatic mutations, and copy number alterations (CNAs). In addition to typical DLBCLs, recognized morphologic and immunophenotypic subtypes include T-cell/histiocyte-rich large B-cell lymphoma and plasmablastic lymphoma (PBL), among others.<sup>1</sup> The transcriptional heterogeneity of DLBCL is addressed by 2 classification schemes, cell of origin (COO) and

consensus clustering classification (CCC).<sup>2-5</sup> Both of these systems highlight specific aspects of DLBCL biology, suggest cancer cell dependencies, and identify rational therapeutic targets.

The COO classification defines DLBCLs that share certain features with normal B-cell subtypes and includes germinal center B-cell (GCB) and activated B-cell (ABC) types.<sup>6,7</sup> GCB-type DLBCLs are tumors derived from light-zone germinal center B cells. *MYC* and *BCL2* translocations are detected in 10% and 40% of these lymphomas, respectively.<sup>6</sup> Additional genetic alterations that occur more frequently in GCB-type DLBCLs include gain-of-function mutations in the chromatin-modifying enzyme *EZH2*<sup>8</sup> and inactivating mutations of

Submitted September 28, 2015; accepted January 11, 2016. Prepublished online as *Blood* First Edition paper, January 15, 2016; DOI 10.1182/blood-2015-09-672352.

\*B.C. and H.C. contributed equally to this study.

†Y.W. and M.A.S. contributed equally to this study.

The online version of this article contains a data supplement.

The publication costs of this article were defrayed in part by page charge payment. Therefore, and solely to indicate this fact, this article is hereby marked "advertisement" in accordance with 18 USC section 1734.

© 2016 by The American Society of Hematology

the G $\alpha$ 13 migration pathway components such as *GNAI3*.<sup>9</sup> In contrast, ABC-type DLBCLs are derived from a germinal center B cell committed to plasmablastic differentiation.<sup>6</sup> ABC-type DLBCLs have increased nuclear factor- $\kappa$ B (NF- $\kappa$ B) activity and more-frequent genetic alterations of certain NF- $\kappa$ B pathway components, including *MYD88* and *CARD11*.<sup>10-12</sup> ABC-type DLBCLs also have more frequent somatic mutations of the genes encoding the immunoglobulin  $\alpha$  or  $\beta$  subunits (*CD79A* or *B*) and associated alterations of B-cell receptor (BCR) surface expression and signaling.<sup>10</sup> These tumors also exhibit alterations associated with a terminal differentiation block, such as *PRDM1* (*BLIMP1*) deletion.<sup>13</sup>

Additional aspects of DLBCL functional heterogeneity are captured by the CCC system, which categorizes DLBCLs purely on the basis of the tumor transcriptome and defines BCR, oxidative phosphorylation (OxPhos), and host response (HR) subtypes.<sup>2,4,5</sup> The BCR-type DLBCLs have more abundant expression of proximal components of the BCR pathway and increased reliance on proximal BCR signaling and survival pathways.<sup>5,14</sup> These tumors include BCR-dependent ABC-type DLBCLs with high baseline NF- $\kappa$ B activity and BCR-dependent GCB-type DLBCLs with low baseline NF- $\kappa$ B activity that largely rely on spleen tyrosine kinase (SYK)/phosphatidylinositol 3-kinase (PI3K)/protein kinase B signaling (AKT).<sup>5</sup> The consequences of proximal BCR/SYK/PI3K pathway inhibition differ in BCR-dependent DLBCLs with high or low baseline NF- $\kappa$ B activity (ABC or GCB types, respectively). In BCR-dependent ABC-type DLBCLs, proximal BCR pathway inhibition decreases the abundance of NF- $\kappa$ B target genes, including antiapoptotic BCL2 family members such as BCL2-related protein A1 (BCL2A1, also known as BFL1/A1).<sup>5</sup> In contrast, proximal BCR pathway inhibition induces the proapoptotic BH3 family member HRK in BCR-dependent GCB-type DLBCLs.<sup>5</sup> BCR-type DLBCLs exhibit additional genetic alterations of proximal BCR pathway components, including copy gain of *SYK* and copy loss of the PI3K negative regulator *PTEN*.<sup>5</sup> BCR-independent OxPhos-type DLBCLs exhibit enhanced mitochondrial energy transduction and selective reliance on fatty acid oxidation.<sup>4</sup> HR-type DLBCLs have a characteristic inflammatory/immune cell infiltrate and include the morphologically defined subset of T-cell/histiocyte-rich B-cell lymphomas.<sup>2</sup>

Additional genetic features of DLBCL are not associated with transcriptionally defined subtypes, including frequent CNAs of p53/cell cycle pathway components and less common somatic mutations of *TP53*, gain-of-function mutations in the BCL6-modulator *MEF2B*, and perturbations of antigen presentation machinery and chromatin modification.<sup>6,15-17</sup>

Despite advances in the molecular and functional characterization of DLBCL, newly diagnosed patients are still largely treated with the same empiric rituximab plus cyclophosphamide/doxorubicin/vincristine/prednisolone (R-CHOP) regimen. Although up to 60% of DLBCL patients are successfully treated with this regimen, the remainder have limited therapeutic options and often succumb to their disease.<sup>18</sup> Preclinical model systems that capture the genetic and functional heterogeneity of primary DLBCL are urgently needed. DLBCL cell lines and associated xenografts are routinely used to analyze rational targets and candidate inhibitors; however, these are imperfect models of the disease. For example, almost all DLBCL cell lines have inactivating somatic mutations of *TP53*, whereas only ~20% of primary DLBCLs have this alteration.<sup>15,19-22</sup>

Although genetically engineered mouse models have revealed mechanistic insights into single genes and pathways,<sup>13,23-26</sup> they do not capture the genetic, transcriptional, and functional heterogeneity of primary human DLBCL. Moreover, these mouse models have variable penetration and time of onset, making them suboptimal systems for

drug development. Patient-derived xenograft (PDX) models<sup>27-32</sup> of primary DLBCLs should overcome these limitations and provide more reflective and reliable models of the disease. However, establishing PDX models of DLBCL has been historically difficult. We have reevaluated and optimized the generation of large B-cell lymphoma (LBCL) PDX models using more-immunocompromised hosts and newer inoculation strategies. Herein, we report both the establishment and the genetic and biological characterization of a series of 9 human LBCL PDX models that capture the heterogeneity of the disease.

## Patients, materials, and methods

### Patient specimens and animals

DLBCL patient specimens were obtained from the British Columbia Cancer Agency with written informed patient consent, following a protocol approved by the Clinical Research Ethics Board of the University of British Columbia. Six- to 8-week-old male NOD SCID IL2R $\gamma$ <sup>null</sup> (NSG) mice (The Jackson Laboratory) were used for the establishment of PDX models. All related experimental protocols were approved by the University of British Columbia Animal Care Committee and the Dana-Farber Cancer Institute Animal Care and Use Committee.

### Development of PDX models

Subrenal capsule PDX models were generated as previously described.<sup>33,34</sup> Surgically removed patient tumor tissue was collected and stored in 4°C Hanks balanced salt solution supplemented with antibiotics and transported to the animal facility within 2 hours of surgery. Each fresh tumor sample was cut into multiple 1 × 2 × 3 mm<sup>3</sup> pieces and kept in sterile Hanks balanced salt solution until it was xenotransplanted. Mouse surgery was performed in a biosafety level 2 laminar flow hood under sterile conditions. An incision of ~1.0 cm was made along the midline of the back of an anesthetized mouse, followed by the opening of the mouse body wall above 1 kidney. Subsequently, the kidney was mechanically pressed through the incision. With the exteriorized kidney resting on the body wall opening, a 2- to 3-mm kidney membrane incision was made with a pair of spring-loaded scissors. Thereafter, a small pocket was created between the kidney membrane and parenchyma using a glass pipette dissector. Then, the primary tumor piece was inserted under the renal capsule and the kidney was gently eased back into the body cavity. The edges of the body wall and skin were aligned and closed with 5-0 surgical threads. Six to 8 male NSG mice were implanted with each primary LBCL.

After xenotransplantation, animals were evaluated regularly for palpable tumors. When tumors were palpable, the animals were euthanized, and tumors were excised and passaged to another cohort of animals. In the described PDX models, the median time to palpable tumor was 45 days (range, 18-257 days). Each graft was serially passaged 5 times by subrenal capsule transplant to generate a stable PDX model. For each LBCL PDX model, tumor tissue was excised, and DNA and RNA were extracted as previously described.<sup>15</sup>

### Whole-transcriptome sequencing (RNA-seq)

**Library preparation and sequencing.** Sequencing libraries were prepared from total RNA samples using Illumina TruSeq RNA Sample Preparation Kit v2 following standard protocols (supplemental Methods, available on the *Blood* Web site).

**Demultiplexing, mapping, and filtering of mouse reads and generation of an expression matrix.** The raw sequencing reads from a lane were demultiplexed with CASAVA 1.8 (Illumina), and aligned to the human (hg19) and mouse (mm10) reference genomes using the TopHat aligner (version 2.0.4).<sup>35</sup> Reads aligned to the mouse genome were filtered out by a custom Perl script. After removing the aligned murine reads, sequences aligned to the human genome were used to generate an expression matrix with cufflinks (version 2.0.2) and the hg19 genes gene-transfer-format file from the University of California, Santa Cruz.

### Gene set enrichment analysis and visualization

Gene set enrichment analysis was performed as previously described<sup>36</sup> using recently reported ABC- and GCB-signature gene sets.<sup>37</sup> Gene expression matrices and nonsynonymous mutations were visualized using GENE-E (<http://www.broadinstitute.org/cancer/software/GENE-E/>).

### Whole exome sequencing (WES)

**Library preparation and sequencing.** Libraries were prepared as previously described<sup>38</sup> using genomic DNAs from the 9 primary LBCLs, 9 tumor specimens from the associated PDX models, 1 NSG mouse (germline), and 2 human (Centre d'Etude du Polymorphisme Humain; Utah residents with ancestry from northern and western Europe; <http://hapmap.ncbi.nlm.nih.gov/citinghapmap.html>) normal, and then sequenced (supplemental Methods).

**Demultiplexing, mapping, and SNV, indel, and rearrangement calling.** Samples sequenced in the same lane were demultiplexed using the Picard tools. Read pairs were aligned to the hg19 reference sequence using the Burrows-Wheeler Aligner,<sup>39</sup> and data were sorted and duplicate-marked using Picard. Bias in base-quality score assignments due to flow cell, lane, dinucleotide context, and machine cycle were analyzed and recalibrated, and local realignment around insertions or deletions (indels) was performed using the Genome Analysis Toolkit.<sup>40,41</sup> Mutation analysis for single-nucleotide variants (SNVs) was performed using MuTect v1.1.4,<sup>42</sup> and indel calling was performed using the Genome Analysis Toolkit SomaticIndelDetector tool. SNV and indel calls were further filtered against variants identified in the mouse control sample to remove calls originating from residual mouse DNA in the PDX tumor specimens. Structural variants were detected using BreakMer.<sup>43</sup> SNVs and indels were annotated using Variant Effect Predictor.<sup>44</sup> For the comparison of primary tumors and associated PDX models, mutant allele fractions of previously reported DLBCL SNVs were plotted (supplemental Table 2A<sup>19-22</sup>). This analysis was restricted to variants that were absent in mouse and unpaired human normal samples and had an allele fraction of >0.1 and coverage of at least 30× in at least 1 of the primary tumors or the PDX models.

### Additional methods

Detailed descriptions of Epstein-Barr-encoded small RNA (EBER) in situ hybridization, immunoglobulin clonality analysis, immunohistochemistry, cell culture, DNA extraction, preparation of libraries for RNA-seq and WES, assessment of *CDKN2A* and *TP53* CNAs, generation of single-tumor cell suspensions, detection of cell surface immunoglobulin expression, and assessment of proliferation and HRK and BCL2A1 transcript abundance after chemical SYK inhibition are included in the supplemental Methods.

## Results

### Establishment of 9 LBCL PDX models

To develop the PDX models, fresh tumor biopsy samples from 28 primary LBCLs were implanted under the renal capsule of immunocompromised NSG mice. After expansion in vivo, xenotransplanted lymphomas were serially transplanted in additional cohorts of NSG mice. With this approach, 9 of 28 (32%) of the primary LBCLs were propagated for ≥5 generations and considered to be stable LBCL PDX models (Figure 1A). In 5 of 9 PDX models, mice with palpable implanted tumors were found to have pulmonary metastases when euthanized.

To rule out expansion of an EBV-infected cell population, we assessed the EBV status of the subrenal tumor from each PDX model using EBER in situ hybridization. All established PDX models were EBV negative (Figure 1B).

In addition, we assessed the B-cell origin and clonality of each PDX model with a PCR assay targeting the V<sub>H</sub>-J<sub>H</sub> region of the heavy chain immunoglobulin locus (Figure 1C).<sup>45</sup> Models LTL-013, -014, -025, -026, -030, and -034 were confirmed to be clonal with the *IgH* V<sub>H</sub>-J<sub>H</sub> FR2 PCR (Figure 1C, left); models LTL-005 and -048 were found to be clonal and model LTL-037 was found to be biclonal with the *IgH* V<sub>H</sub>-J<sub>H</sub> FR1 PCR assay (Figure 1C, right).

### IHC characterization of the LBCL PDX models

After establishing 9 clonal EBV<sup>−</sup> LBCL PDX models, each tumor was evaluated with a panel of immunohistochemical (IHC) markers (hematoxylin and eosin, CD20, CD10, MUM1 (IRF4), BCL6, BCL2, and MYC) (Figure 2; Table 1). The morphology and IHC signatures of 8 LBCL PDX models were consistent with the diagnosis of DLBCL (Figure 2A). Each of the DLBCL PDX models had a representative but model-specific pattern of CD10, BCL6, MUM1, BCL2, and MYC expression (Figure 2A; Table 1). All eight DLBCL PDX models were positive for CD20, although LTL-014 expressed CD20 on only 5% of cells. PDX model LTL-037 had 2 populations by CD20 intensity (Figure 2A), consistent with the biclonal *IgH* analysis (Figure 1C).

The LTL-048 PDX model was a CD20<sup>−</sup>/MUM1<sup>+</sup>/BCL6<sup>−</sup> clonal B-cell tumor with concurrent expression of CD79a and clonal restriction of intracytoplasmatic κ light chain, features indicative of an EBV<sup>−</sup> PBL (Figure 2B).<sup>46</sup>

### Transcriptional heterogeneity within the LBCL PDX models

We next sought to classify the LBCL PDX models with respect to the COO and CCC transcriptional subtypes.<sup>2,3</sup> All LBCL PDX models were subjected to RNA-seq. We hypothesized that the infiltrating murine cells in the PDX tumors (Figure 1A) might interfere with RNA-based classification models, especially because RNA-seq protocols select for poly(A)-containing transcripts that are highly conserved between mouse and human. For this reason, we first estimated the percentage of murine transcripts in each PDX model by counting the reads aligned to the mouse reference genome (5.6%-37% of all aligned sequences) (supplemental Figure 1). We then removed the reads aligned to the mouse genome in each model before generating the expression matrix and classifying the PDX models into COO and CCC subtypes.<sup>2,3,47</sup>

With this approach, of the 8 DLBCL PDX models, 6 were classified as ABC type and 2 were defined as GCB type (Table 2; Figure 3A). Consistent with their COO transcriptional signatures, the 6 ABC-type



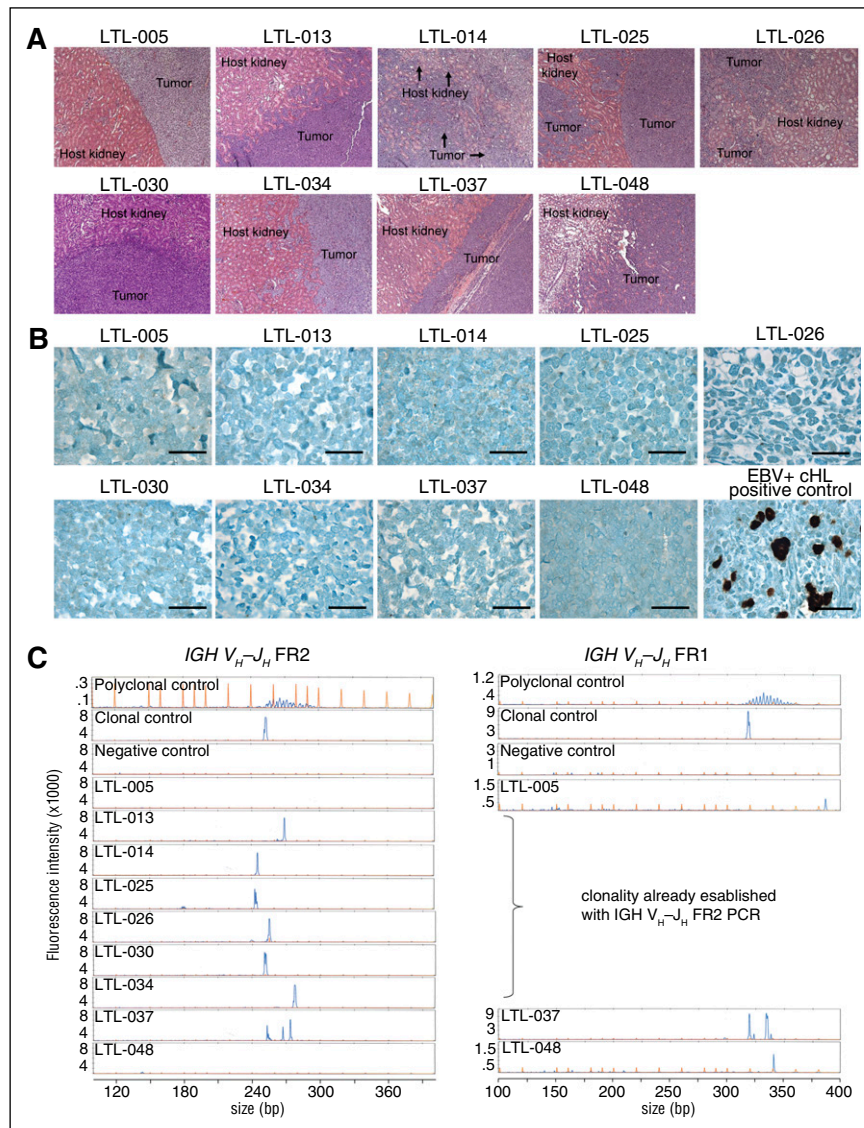


**Figure 1. Establishment of 9 LBCL PDX models.** (A) Hematoxylin and eosin stains of 9 LBCL PDX models propagated under the renal capsule of NSG mice. Original magnification  $\times 200$ . (B) Epstein-Barr-encoded RNA in situ hybridization of all 9 LBCL PDX models. An EBV-positive classical Hodgkin lymphoma (cHL) served as positive control. Bars represent 100  $\mu\text{m}$ . (C) Clonality of the 9 PDX models assessed and interpreted according to the EuroClonality/BIOMED-2 guidelines.<sup>45</sup> An *IgH*  $V_H$ - $J_H$  spanning PCR (FR2, left) was performed on all 9 LBCL PDX models. Tumors without a clonal peak (LTL-005, LTL-037, and LTL-048) or an inconclusive result (LTL-037) were sequentially analyzed with a second PCR (FR1, right). Genomic DNA (gDNA) of NSG mouse tail served as a negative control, gDNA of peripheral blood mononuclear cells from a healthy human volunteer served as a polyclonal control, and gDNA of the Burkitt lymphoma cell line (BL30) served as a monoclonal control. EBV, Epstein-Barr virus; FR, fragment; PCR, polymerase chain reaction.

PDX models expressed increased MUM1, and the 2 GCB tumors had higher CD10 protein levels by IHC (Figure 2A). To further characterize the predicted GCB- and ABC-type DLBCL PDX models, we performed gene set enrichment analyses using recently reported ABC- and GCB-signature gene sets<sup>37</sup> (Figure 3B). The respective signatures were significantly enriched in the predicted PDX models (ABC signature in ABC-type PDX models,  $P < .001$ ; GCB signature in GCB-type PDX models,  $P = .01$ ; Figure 3B). The PBL PDX model did not exhibit selective expression of specific COO markers, consistent with its unique biology (Figure 3A). Using the CCC classification, 6 of 8 DLBCL PDX models (both of the GCB-type DLBCLs and 4 of 6 ABC-type DLBCLs) were classified as BCR subtype, whereas the remaining 2 PDX models were of non-BCR type (Table 2).

#### Genetic characterization of LBCL PDX models

To gain insight into the genetic alterations in each LBCL PDX model, we subjected PDX tumor specimens and an NSG mouse germline control to WES. The classical WES bait set was extended with baits spanning 39 chromosomal regions that are rearranged in specific hematologic malignancies (supplemental Table 1A). We first estimated

the murine contribution to the LBCL PDX WES data and determined the median mouse sequences to be  $\sim 3.4\%$  of total reads. There were relatively fewer murine reads in the WES data than in the RNA-seq data, likely due to the specific design of the WES bait set.

#### Chromosomal rearrangements in the LBCL PDX models.

To detect chromosomal rearrangements, the DNA-sequencing data (WES plus custom bait set) for each PDX model was analyzed with the BreaKmer algorithm.<sup>43</sup> Chromosomal translocations were detected in 2 of the PDX models:  $t(8;14)/IgH-MYC$  in LTL-014 and  $t(14;18)/IgH-BCL2$  in LTL-030 (Figure 3C; supplemental Table 1B). In both cases, the chromosomal translocations juxtaposed either the *BCL2* or the *MYC* locus to strong *IgH* enhancer elements (Figure 3C). Of note, the breakpoint in the  $t(14;18)/IgH-BCL2$  translocation places the *IgH* enhancer  $\sim 6$  kb distal to the end of the *BCL2* gene between the major and minor breakpoint regions, as previously described in primary tumor specimens.<sup>48</sup> Consistent with these genetic alterations, the PDX models with the highest *MYC* and *BCL2* expression were LTL-014 and LTL-030, respectively (Figure 2A). The  $t(14;18)/IgH-BCL2$  translocation occurred in a GCB-type DLBCL PDX model (LTL-030), as reported in primary DLBCL.<sup>7</sup> Of interest, the  $t(8;14)/IgH-MYC$  translocation



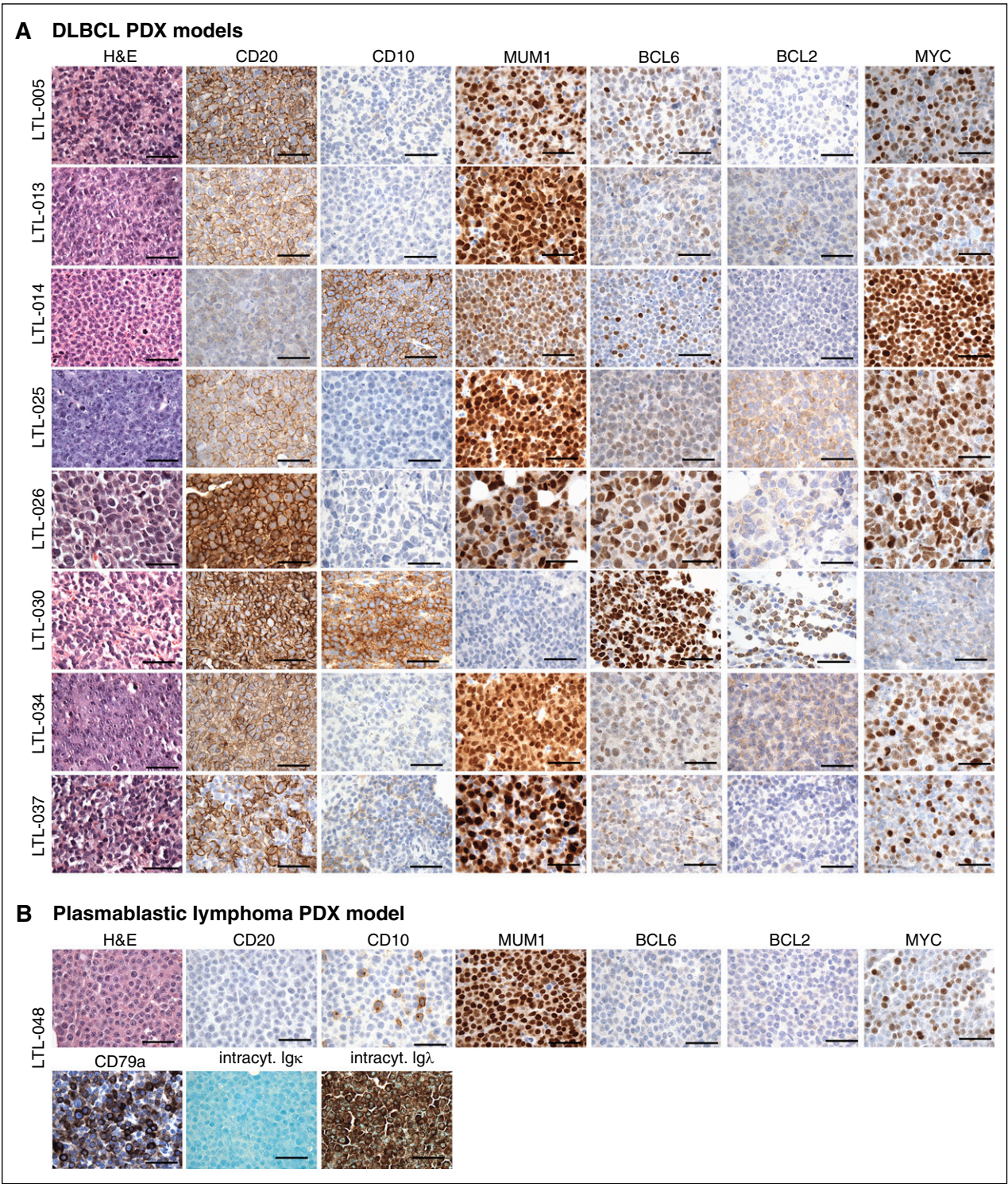


**Figure 2. IHC characterization of all 9 PDX models.** (A) IHC analyses of the indicated markers in all 8 DLBCL PDX models, which were consistent with the diagnosis of DLBCL. (B) IHC assessment of indicated markers in PDX model LTL-048, which is consistent with the diagnosis of PBL. Scale bars, 100  $\mu$ m. See also Table 1. intracyt., intracytoplasmic.

occurred in the second GCB-type DLBCL PDX model, suggesting that both GCB-type models required additional genetic drivers for murine engraftment. In primary DLBCLs, *BCL2* and *MYC* translocations are known adverse prognostic features in GCB-type tumors.<sup>49-53</sup> We also noted that the DLBCL PDX model with the t(8;14)/*IgH-MYC* translocation (LTL-014) had only 5% CD20-positive cells (Figure 2; Table 1).

**Mutations in the LBCL PDX models.** After applying a rigorous filter to remove common human or mouse single-nucleotide polymorphisms, we next queried for the most frequently reported recurrent mutations in primary DLBCLs (mutations identified as significant in 2/4 publications<sup>19-22</sup>; supplemental Table 2). Mutations present in at least 1 DLBCL PDX model are included in Figure 3D and supplemental Table 2C.



**Table 1. Clonality, and IHC characterization of the LBCL PDX models**

Model ID	Clonality	Diagnosis	IHC, % (intensity)					
			CD20	CD10	MUM1	BCL6	BCL2	MYC
LTL-005	Yes (mono, FR1)	DLBCL	100	Negative	70 (3+)	60 (2+)	Negative	40
LTL-013	Yes (mono, FR2)	DLBCL	90	Negative	10 (3+)	20 (1+)	10 (1+)	80
LTL-014	Yes (mono, FR2)	DLBCL	5	90 (2+)	80 (2+)	30 (2+)	Negative	99
LTL-025	Yes (mono, FR2)	DLBCL	100	Negative	100 (3+)	40 (1+)	90 (2+)	90
LTL-026	Yes (mono, FR2)	DLBCL	100	Negative	50 (3+)	80 (2+)	70 (1+)	90
LTL-030	Yes (mono, FR2)	DLBCL	100	100 (2+)	Negative	90 (3+)	90 (3+)	10
LTL-034	Yes (mono, FR2)	DLBCL	100	Negative	100 (3+)	50 (1+)	9 (1+)	70
LTL-037	Yes (bi, FR1)	DLBCL	70*	Negative	70 (3+)	Negative	Negative	40
LTL-048	Yes (mono, FR1)	PBL	Negative	20 (1+)	100 (3+)	Negative	Negative	50

\*Two populations by CD20 intensity.

One of the GCB-type DLBCL PDX models, LTL-030, had alterations of *GNAI3*, *CREBBP*, and *EZH2*, all previously linked to the GCB subtype.<sup>9,20,21</sup> ABC-type DLBCL PDX models had a larger spectrum of mutations, including *MYD88* in association with *CARD11* and *CD79B* (LTL-013), *PIM1* (LTL-005), or *PRDM1* (LTL-034), or *CD79B* with additional alterations (LTL-026), as previously reported in primary ABC-type DLBCLs.<sup>10,12,20,21</sup> Certain PDX models had additional mutations, including *B2M*, *MLL2*, *MEF2B*, *NOTCH1*, and *TP53*.<sup>16,17,20,21,54</sup> None of the 37 most recurrently mutated genes in DLBCL was identified in the PBL PDX model.

Importantly, we found that only 25% (2/8) of the DLBCL PDX models harbored inactivating *TP53* mutations (Figure 3D). This finding is consistent with the reported incidence of *TP53* mutations in primary DLBCLs<sup>15,19-22,55</sup> and unlike the near-uniform presence of *TP53* somatic mutations in DLBCL cell lines.<sup>15</sup>

**CNAs of *TP53* and *CDKN2A*.** We previously reported that primary DLBCLs often exhibit CNAs of *TP53* or additional modifiers of the p53 pathway in addition to less frequent somatic mutations of *TP53*.<sup>15</sup> For this reason, we used a targeted real-time PCR assay to assess copy numbers of *TP53* and its upstream modifier, *CDKN2A*, in the PDX models (Figure 3D). Five of the 8 DLBCL PDX models (LTL-005, LTL-013, LTL-014, LTL-025, and LTL-026) exhibited single copy loss of *TP53*. In LTL-013 and LTL-014, this resulted in functional biallelic inactivation of *TP53* because the second *TP53* allele was inactivated by somatic mutation (Figure 3D). Because the *CDKN2A* locus encodes 2 alternative transcripts, p16<sup>INK4A</sup> and p19<sup>ARF</sup>, we assessed the *CDKN2A* locus with 3 separate copy number assays that covered the representative exons in each transcript. Two of the PDX models (LTL-025 and LTL-034) had complete loss of all coding exons of *CDKN2A*, and an additional model (LTL-005) lost both copies of the p16<sup>INK4A</sup>-encoding portion of the gene. Two additional PDX models (LTL-026 and LTL-014) had single copy loss of the coding *CDKN2A* exons. Overall, we detected CNAs of *TP53* or *CDKN2A* in 75% (6/8) of the DLBCL PDX models and detected somatic *TP53* mutations in only 25% (2/8) of models, similar to the reported incidence of p53 pathway alterations in primary DLBCLs.<sup>15</sup>

**Genetic stability of PDX models.** To evaluate the genetic stability of the PDX models, we compared genetic alterations in each primary LBCL with its associated PDX model. We employed WES with the same extended bait set to capture all mutations perturbing the protein sequence and selected chromosomal rearrangements. The identical chromosomal rearrangements of *IgH/MYC* (LTL-14) or *IgH/BCL2* (LTL-030) were detected at base-pair resolution in the primary tumors and associated PDX models (supplemental Figure 2).

We also compared the mutant allele fraction (frequency of a mutation at a particular locus) in each of the primary tumors and

associated PDX models (Figure 4; supplemental Table 2A<sup>19-22</sup>). The majority of DLBCL SNVs were present at similar mutant allele fractions in the PDX models and the original primary tumors (Figure 4). For example, the mutant allele fractions of almost all DLBCL SNVs were comparable in LTL-005, LTL-013, LTL-026, and LTL-037 primary tumors and PDX models. In certain models, select DLBCL SNVs were more common in the PDX model than in the primary tumor (*TP53* in LTL-014, *KMT2D* [*MLL*] and *TMEM30A* in LTL-025, *B2M* and *MEF2B* in LTL-030, and *PRDM1* [*BLIMP1*] in LTL-034). Mutant allele fractions of hallmark DLBCL SNVs, including *MYD88*, *PIM1*, *CARD11* and *CD79B*, *TNFAIP3*, *EZH2*, and *POUZF2*, were similar in the primary tumors and PDX models. Of note, 2 common DLBCL SNVs were detected in the primary tumors but not in the PDX models (*GNAI3* in LTL-014 and *TP53* in LTL-037). These data provide further evidence that the PDX models largely capture and retain the genetic heterogeneity of the primary DLBCLs.

### Assessing integrity of BCR signaling in PDX models

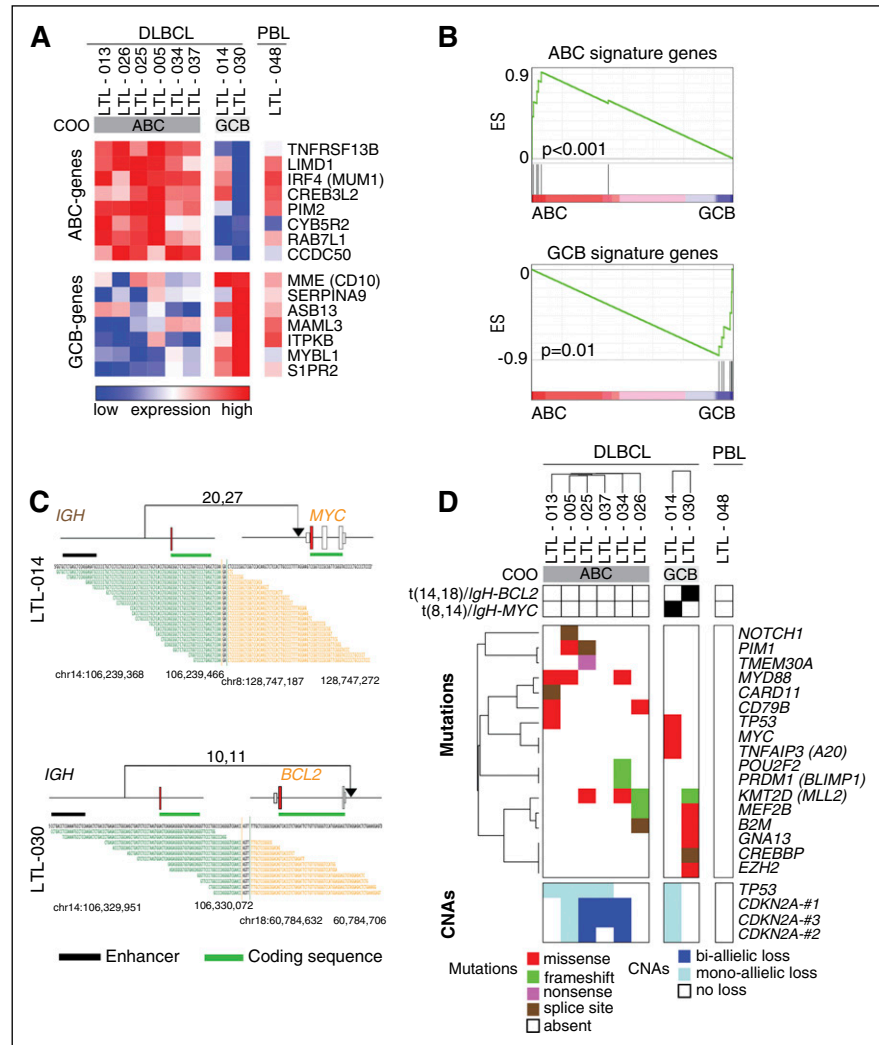
After establishing and genetically characterizing the 9 LBCL PDX models, we assessed their utility for functional analyses of BCR signaling. To this end, we excised subrenal tumor from each of the PDX models, generated viable tumor cell suspensions, and assessed surface immunoglobulin expression by flow cytometry (Figure 5A). Six of the 8 DLBCL PDX models had expression of surface IgM, suggesting that these models derived from non-class-switched GCBs (Figure 5A). The remaining 2 DLBCL PDX models and the PBL PDX model had no surface IgM expression; none of the PDX models had surface IgG expression (Figure 5A). Of interest, all of the surface immunoglobulin-positive LBCL PDX models were classified as

**Table 2. Transcriptional subtypes of the DLBCL PDX models**

Model ID	COD	CCC
LTL-005	ABC	BCR
LTL-013	ABC	BCR
LTL-014	GCB	BCR
LTL-025	ABC	BCR
LTL-026	ABC	BCR
LTL-030	GCB	BCR
LTL-034	ABC	HR
LTL-037	ABC	OxPhos

All DLBCL PDX models were classified using COO and CCC criteria.<sup>3,15</sup>

**Figure 3. Molecular heterogeneity of LBCL PDX models.** (A) Heatmap of the relative expression of ABC- and GCB-signature genes<sup>37</sup> in ABC- and GCB-type DLBCL PDX models and the additional PBL PDX model. Note that reads aligned to the mouse genome were filtered before the DLBCL PDX models were classified by COO.<sup>3</sup> (B) Gene set enrichment analyses of the ABC-signature genes (upper) and GCB-signature genes (lower) in the ABC- and GCB-type DLBCL PDX models. (C) Detected *IGH-MYC* (upper) and *IGH-BCL2* (lower) translocations in LTL-014 and LTL-030, respectively. Translocations are plotted in their genomic context. Exons are visualized as boxes, with ATG-containing exons in red, coding regions underlined in green, and enhancer regions underlined in black. Numbers of supporting reads (split reads, read pairs) are indicated above, and individual supporting reads are shown below. (D) Protein-perturbing mutations with an allele fraction >0.1 in the LBCL models. Mutations in most frequently reported recurrently mutated genes in primary DLBCL (supplemental Table 2C) are visualized as a color-coded heatmap (red, missense mutation; green, frameshift mutation; purple, nonsense mutation; brown, splice site mutation; white, mutation absent); CNAs in *TP53* and *CDKN2A* are represented as a color-coded heatmap (dark blue, biallelic loss; light blue, monoallelic loss; white, no loss). COO transcriptional subtypes and identified translocations juxtaposing either *BCL2* or *MYC* to the *IgH* locus are indicated in the legend above of the heatmap. ES, enrichment score.



BCR-type DLBCLs by CCC.<sup>5</sup> These surface immunoglobulin-positive BCR-type DLBCLs belonged to both COO subtypes (GCB-type: LTL-014 and LTL-30; ABC-type: LTL-005, LTL-013, LTL-025, and LTL-026; Figure 5A).

Next, we assessed the functional integrity of BCR signaling in the panel of LBCL PDX models using the selective SYK inhibitor entospletinib (GS-9973), which is currently in clinical trials for multiple B-cell malignancies.<sup>56-58</sup> Like other chemical SYK inhibitors and molecular SYK depletion,<sup>5</sup> single-agent entospletinib (GS-9973) selectively blocked the proliferation of BCR-dependent DLBCL cell lines, abrogated the phosphorylation of SYK (pSYK<sup>525/526</sup>) and downstream pathway components, and modulated the expression of specific BCL2 family members (HRK and BCL2A1) in BCR-dependent DLBCL cell lines with low- and high baseline NF- $\kappa$ B activity (supplemental Figure 3).

In single-cell suspensions of the LBCL PDX tumors, entospletinib treatment significantly decreased the proliferation of all 6 BCR-type DLBCLs but had no effect on the non-BCR-type DLBCLs or the PBL (Figure 5B). Given the distinctive SYK/PI3K-dependent signaling and survival pathways in DLBCLs with low or high baseline NF- $\kappa$ B, which largely correspond to BCR-dependent GCB- or ABC-type DLBCLs, respectively,<sup>5</sup> we next assessed readouts of these

pathways (Figure 5C-D). As in DLBCL cell lines (supplemental Figure 3) and primary DLBCL patient samples,<sup>5</sup> chemical SYK inhibition selectively induced the proapoptotic BH3-only family member HRK in both of the BCR-dependent GCB-type DLBCL PDX samples (Figure 5C) and decreased expression of the antiapoptotic BCL2-family member BCL2A1 in BCR-dependent ABC-type DLBCL PDX tumors (Figure 5D). These data indicate that the molecularly characterized DLBCL PDX models faithfully reflect defined differences in BCR dependence, downstream signaling, and survival pathways.

## Discussion

We have generated and characterized a panel of LBCL PDX models, including 8 that reflect the immunophenotypic, transcriptional, genetic, and functional heterogeneity of primary DLBCL. One additional model is of the immunophenotypically and morphologically distinct LBCL subtype, PBL.<sup>45</sup> These data indicate that implanting fresh LBCL specimens within the highly vascularized subrenal capsule of immunodeficient mice is feasible and effective, as reported for certain solid tumors.<sup>33,34</sup>

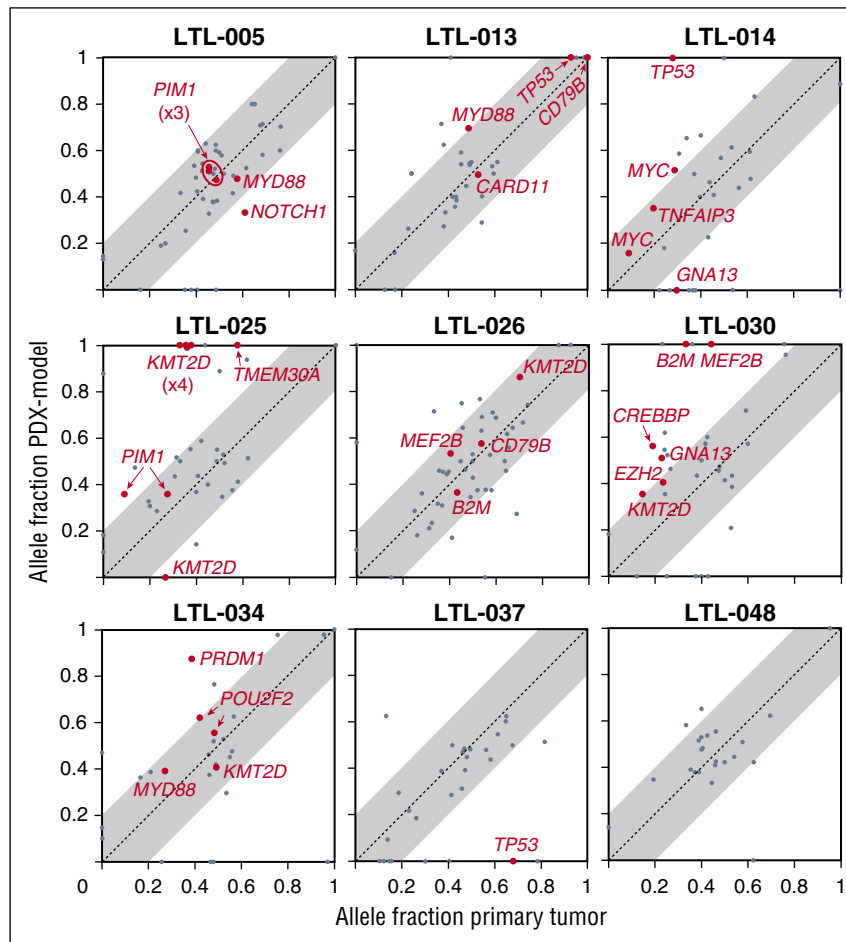


**Figure 4. Comparison of mutant allele fraction between primary tumor and associated PDX model.** We plotted the mutant allele fraction (frequency of a mutation at a particular locus) in the primary tumors (x-axis) and the associated PDX models (y-axis). SNVs in genes reported to be mutated in at least 1 of 4 DLBCL sequencing series are represented in gray, and SNVs in genes reported to be mutated in at least 2 of 4 DLBCL sequencing series are labeled in red (supplemental Table 2A<sup>19-22</sup>). Multiple SNVs in the same gene are noted (*PIM1* in LTL-005, *KMT2D* in LTL-025, and *POU2F2* in LTL-034). Mutant allele fractions along the diagonal ( $x = y$ , identical mutant allele fractions, dotted line) indicate similar clonal frequencies in the primary tumor and associated PDX model. Mutant alleles that are more abundant in the PDX model than in the primary tumors are above the diagonal. Allele fractions  $\pm 0.2$  from the identical mutant allele fractions are visualized in gray.

Our genomic characterization of human PDX models revealed the importance of computationally subtracting murine reads in RNA-seq data. RNA-seq data contained a higher percentage of murine reads than DNA-sequencing data (WES), likely due to the associated differences in library preparation. For these reasons, we eliminated mouse-specific reads from our RNA-seq data before characterizing the transcriptional signatures of the LBCL PDX models and used the DNA-seq data to call mutations and chromosomal rearrangements. These approaches to the analysis of transcriptional signatures and mutation calling will be broadly applicable across tumor types.

Applying the RNA-based COO classification to the DLBCL PDX series, 6 of 8 models were classified as ABC type and 2 as GCB type. The higher engraftment rate of ABC-type DLBCL PDX models may reflect the more aggressive course of the clinical disease.<sup>59</sup> Of interest, 5 of 6 ABC-type PDX models had additional genetic alterations of p53/cell cycle pathway components, including 3 models with biallelic loss of *CDKN2A*, 1 model with biallelic inactivation of *TP53* (mutation and single copy loss), and another model with single copy loss of *TP53*. Furthermore, the 2 GCB-type PDX models had additional adverse genetic features: t(14;18)/*IgH-BCL2* translocation or t(8;14)/*IgH-MYC* translocation.<sup>49-53</sup> The GCB-type PDX model with the *MYC* translocation also had biallelic inactivation of *TP53* (mutation and single copy loss). In this initial series of DLBCL PDX models, tumors with more aggressive genetic features are overrepresented, suggesting that such lymphomas may engraft more readily in NSG mice. These

findings are consistent with those in solid tumors in which engraftment and PDX generation were adversely associated with patient overall survival.<sup>27,60</sup>

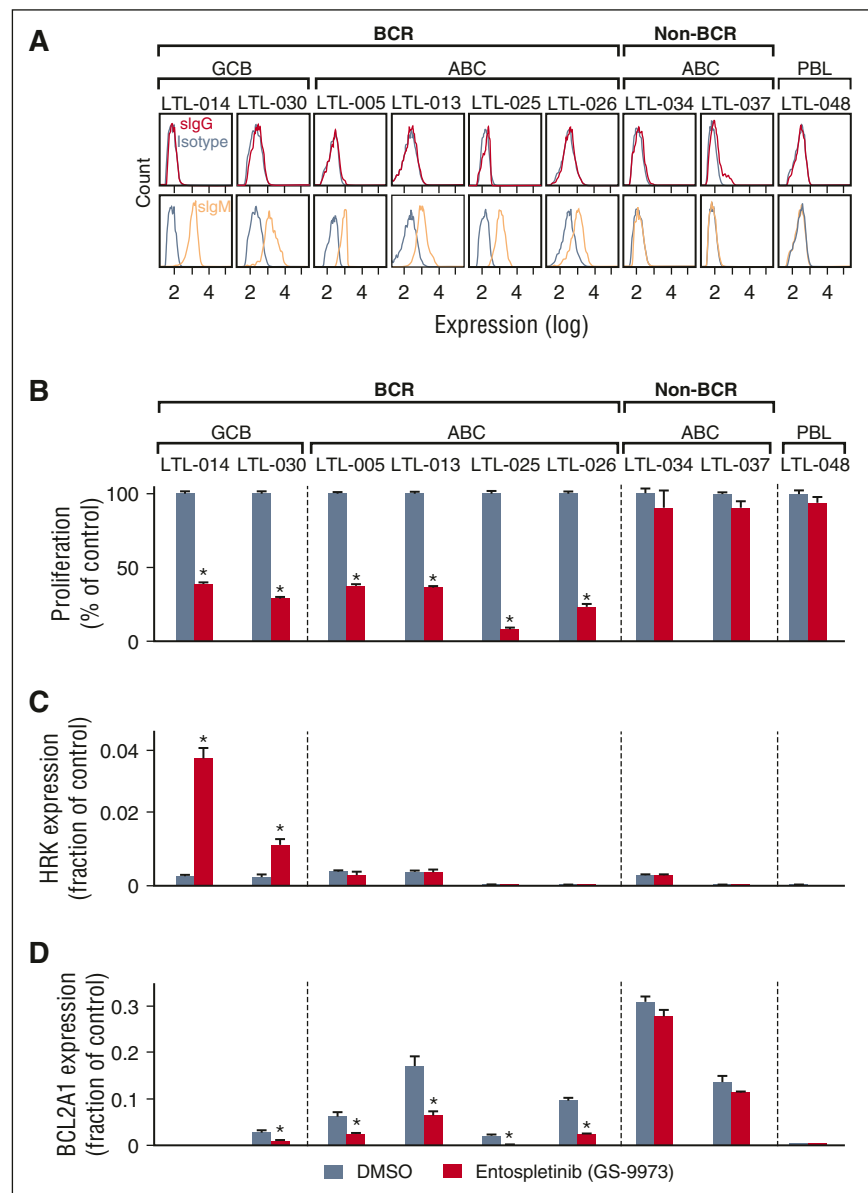
By performing WES of the DLBCL PDX models, we identified mutations associated with COO subtype (ABC: *MYD88*, *CD79B*, *CARD11*, and *PIM1*<sup>10,12,21</sup>; GCB: *GNA13*, *EZH2*, and *CREBBP*<sup>8,9,61</sup>) and additional reported alterations (*B2M*, *MLL2*, *TNFAIP3*, and *MEF2B*).<sup>6,15-17</sup> Only 25% (2/8) of the DLBCL PDX models harbored inactivating *TP53* mutations, whereas 75% (6/8) of tumors exhibited CNAs of *TP53* or its upstream modifier, *CDKN2A*. These data are consistent with the reported incidence and type of *TP53* alterations in primary DLBCLs and contrast sharply with the near-uniform presence of inactivating *TP53* mutations in DLBCL cell lines.<sup>15</sup> For these reasons, the DLBCL PDX panel may be particularly useful for the analysis of p53 mimetics<sup>62</sup> or MDM2/MDM4 inhibitors<sup>63</sup> which require wild-type p53 activity.

By comparing the mutant allele fraction in primary LBCLs and the associated PDX models, we were able to assess the stability of the PDX genetic signature. Most of the LBCL mutations were present at similar allele fractions in the PDX models and the associated primary tumors, indicating that these models largely retain the complex genetic signature of primary LBCLs.

As noted, 6 of the DLBCL PDX models were identified as BCR type based on CCC transcriptional profiles, including 4 ABC-type and 2 GCB-type tumors. The BCR-type DLBCLs were selectively surface IgM positive and sensitive to chemical inhibition of SYK



**Figure 5. Analyses of cell surface immunoglobulin and BCR signaling in the LBCL PDX models.** (A) Single-cell suspensions from each LBCL PDX model were gated for human CD45-positive cells and analyzed for surface immunoglobulin (IgG, red; IgM, orange; isotype, gray). CCC and COO subtypes of each model are indicated above the flow histograms. (B) Cellular proliferation of PDX tumor cell suspensions after chemical SYK inhibition with entospletinib (GS-9973) for 24 hours. (C,D) HRK (C) and BCL2A1 (D) transcript abundance following entospletinib (GS-9973) treatment. Experiments were performed in triplicate. A representative experiment of biological duplicates is shown. DMSO, dimethylsulfoxide. The *P* values were obtained using a Student *t* test (\**P* < .05).



using entospletinib. As in our previous studies,<sup>5</sup> the readouts of SYK inhibition differed in BCR-dependent ABC- and GCB-type DLBCL PDX models: downregulation of NF- $\kappa$ B targets such as BCL2A1 in ABC-type tumors vs HRK upregulation in GCB-type tumors. These studies highlight the utility of having a diverse and well-characterized DLBCL PDX panel for evaluating targeted inhibitors of subtype-specific survival programs. In addition, these studies illustrate the usefulness of PDX models as a renewable source of viable tumor cells for the analysis of sensitivity and resistance to novel targeted agents.

In summary, we have established a molecularly characterized and faithful panel of PDX models of primary DLBCL and PBL and demonstrated their usefulness in evaluating proximal BCR pathway inhibition. We anticipate that the panel of LBCL PDX models will facilitate rational target identification and pre-clinical drug discovery. In addition, the associated insights regarding both the establishment and the molecular characterization of the LBCL PDX models will be broadly applicable to other tumor types.

## Acknowledgments

This work was supported by the Claudia Adams Barr Program in Innovative Basic Cancer Research (B.C.), the Terry Fox Research Institute Program Project Grant #1023 (R.D.G.), National Institutes of Health National Cancer Institute grant (P01 CA092625) (M.A.S.) and a Leukemia & Lymphoma Society Translational Research Program award (M.A.S.).

## Authorship

Contribution: B.C. designed and performed the research, analyzed the data, and wrote the paper; H.C., A.W., S.J.R., and Y.W. designed and performed the research and analyzed the data; M.D.D., D.G., L.C., M.G.M.R., J.O., L.Z., Y.T., R.P.A., A.R.T., G.S.P., S.M., and G.G.W. performed the research and analyzed the data; A.L.C., F.v.B., P.F., and

H.H.S. performed the research; P.v.H., J.C.A., R.D.G., and D.M.W. designed the research; and M.A.S. designed the research, analyzed the data, and wrote the paper.

Conflict-of-interest disclosure: D.M.W. received consulting fees and research support from Novartis. M.A.S. has served on advisory

boards for Gilead Sciences. The remaining authors declare no competing financial interests.

Correspondence: Margaret Shipp, Dana-Farber Cancer Institute, Harvard Medical School, 450 Brookline Ave, Mayer 513, Boston, MA 02215; e-mail: [margaret\\_shipp@dfci.harvard.edu](mailto:margaret_shipp@dfci.harvard.edu).

## References

- Freedman AS, Friedberg JW, Aster JC. Classification of the hematopoietic neoplasms. Available at: [www.upToDate.com/contents/classification-of-the-hematopoietic-neoplasms?source=search\\_result&search=Classification+of+the+hematopoietic+neoplasms&selectedTitle=1~150](http://www.upToDate.com/contents/classification-of-the-hematopoietic-neoplasms?source=search_result&search=Classification+of+the+hematopoietic+neoplasms&selectedTitle=1~150). Accessed August 9, 2015.
- Monti S, Savage KJ, Kutok JL, et al. Molecular profiling of diffuse large B-cell lymphoma identifies robust subtypes including one characterized by host inflammatory response. *Blood*. 2005;105(5):1851-1861.
- Wright G, Tan B, Rosenwald A, Hurt EH, Wiestner A, Staudt LM. A gene expression-based method to diagnose clinically distinct subgroups of diffuse large B cell lymphoma. *Proc Natl Acad Sci USA*. 2003;100(17):9991-9996.
- Caro P, Kishan AU, Norberg E, et al. Metabolic signatures uncover distinct targets in molecular subsets of diffuse large B cell lymphoma. *Cancer Cell*. 2012;22(4):547-560.
- Chen L, Monti S, Juszczynski P, et al. SYK inhibition modulates distinct PI3K/AKT-dependent survival pathways and cholesterol biosynthesis in diffuse large B cell lymphomas. *Cancer Cell*. 2013;23(6):826-838.
- Basso K, Dalla-Favera R. Germinal centres and B cell lymphomagenesis. *Nat Rev Immunol*. 2015;15(3):172-184.
- Lenz G, Staudt LM. Aggressive lymphomas. *N Engl J Med*. 2010;362(15):1417-1429.
- Morin RD, Johnson NA, Severson TM, et al. Somatic mutations altering EZH2 (Tyr641) in follicular and diffuse large B-cell lymphomas of germinal-center origin. *Nat Genet*. 2010;42(2):181-185.
- Muppidi JR, Schmitz R, Green JA, et al. Loss of signalling via Gα13 in germinal centre B-cell-derived lymphoma. *Nature*. 2014;516(7530):254-258.
- Davis RE, Ngo VN, Lenz G, et al. Chronic active B-cell-receptor signalling in diffuse large B-cell lymphoma. *Nature*. 2010;463(7277):88-92.
- Lenz G, Davis RE, Ngo VN, et al. Oncogenic CARD11 mutations in human diffuse large B cell lymphoma. *Science*. 2008;319(5870):1676-1679.
- Ngo VN, Young RM, Schmitz R, et al. Oncogenically active MYD88 mutations in human lymphoma. *Nature*. 2011;470(7332):115-119.
- Mandelbaum J, Bhagat G, Tang H, et al. BLIMP1 is a tumor suppressor gene frequently disrupted in activated B cell-like diffuse large B cell lymphoma. *Cancer Cell*. 2010;18(6):568-579.
- Chen L, Monti S, Juszczynski P, et al. SYK-dependent tonic B-cell receptor signaling is a rational treatment target in diffuse large B-cell lymphoma. *Blood*. 2008;111(4):2230-2237.
- Monti S, Chapuy B, Takeyama K, et al. Integrative analysis reveals an outcome-associated and targetable pattern of p53 and cell cycle deregulation in diffuse large B cell lymphoma. *Cancer Cell*. 2012;22(3):359-372.
- Challa-Malladi M, Lieu YK, Califano O, et al. Combined genetic inactivation of β2-Microglobulin and CD58 reveals frequent escape from immune recognition in diffuse large B cell lymphoma. *Cancer Cell*. 2011;20(6):728-740.
- Ying CY, Dominguez-Sola D, Fabi M, et al. MEF2B mutations lead to deregulated expression of the oncogene BCL6 in diffuse large B cell lymphoma. *Nat Immunol*. 2013;14(10):1084-1092.
- Gisselbrecht C, Glass B, Mounier N, et al. Salvage regimens with autologous transplantation for relapsed large B-cell lymphoma in the rituximab era. *J Clin Oncol*. 2010;28(27):4184-4190.
- Lohr JG, Stojanov P, Lawrence MS, et al. Discovery and prioritization of somatic mutations in diffuse large B-cell lymphoma (DLBCL) by whole-exome sequencing. *Proc Natl Acad Sci USA*. 2012;109(10):3879-3884.
- Zhang J, Grubor V, Love CL, et al. Genetic heterogeneity of diffuse large B-cell lymphoma. *Proc Natl Acad Sci USA*. 2013;110(4):1398-1403.
- Morin RD, Mendez-Lago M, Mungall AJ, et al. Frequent mutation of histone-modifying genes in non-Hodgkin lymphoma. *Nature*. 2011;476(7360):298-303.
- Pasqualucci L, Trifonov V, Fabbri G, et al. Analysis of the coding genome of diffuse large B-cell lymphoma. *Nat Genet*. 2011;43(9):830-837.
- Cattoretti G, Pasqualucci L, Ballon G, et al. Deregulated BCL6 expression recapitulates the pathogenesis of human diffuse large B cell lymphomas in mice. *Cancer Cell*. 2005;7(5):445-455.
- Calado DP, Zhang B, Srinivasan L, et al. Constitutive canonical NF-κB activation cooperates with disruption of BLIMP1 in the pathogenesis of activated B cell-like diffuse large cell lymphoma. *Cancer Cell*. 2010;18(6):580-589.
- Greenwald RJ, Tumang JR, Sinha A, et al. E mu-BRD2 transgenic mice develop B-cell lymphoma and leukemia. *Blood*. 2004;103(4):1475-1484.
- Karret FA, Reschke M, Ruocco A, et al. The BRAF pseudogene functions as a competitive endogenous RNA and induces lymphoma in vivo. *Cell*. 2015;161(2):319-332.
- Tentler JJ, Tan AC, Weekes CD, et al. Patient-derived tumour xenografts as models for oncology drug development. *Nat Rev Clin Oncol*. 2012;9(6):338-350.
- Heyer J, Kwong LN, Lowe SW, Chin L. Non-germline genetically engineered mouse models for translational cancer research. *Nat Rev Cancer*. 2010;10(7):470-480.
- Cook N, Jodrell DI, Tuveson DA. Predictive in vivo animal models and translation to clinical trials. *Drug Discov Today*. 2012;17(5-6):253-260.
- Aparicio S, Hidalgo M, Kung AL. Examining the utility of patient-derived xenograft mouse models. *Nat Rev Cancer*. 2015;15(5):311-316.
- Hidalgo M, Amant F, Biankin AV, et al. Patient-derived xenograft models: an emerging platform for translational cancer research. *Cancer Discov*. 2014;4(9):998-1013.
- Day CP, Merlino G, Van Dyke T. Preclinical mouse cancer models: a maze of opportunities and challenges. *Cell*. 2015;163(1):39-53.
- Wang Y, Revelo MP, Sudilovsky D, et al. Development and characterization of efficient xenograft models for benign and malignant human prostate tissue. *Prostate*. 2005;64(2):149-159.
- Lee CH, Xue H, Sutcliffe M, et al. Establishment of subrenal capsule xenografts of primary human ovarian tumors in SCID mice: potential models. *Gynecol Oncol*. 2005;96(1):48-55.
- Trapnell C, Pachter L, Salzberg SL. TopHat: discovering splice junctions with RNA-Seq. *Bioinformatics*. 2009;25(9):1105-1111.
- Subramanian A, Tamayo P, Mootha VK, et al. Gene set enrichment analysis: a knowledge-based approach for interpreting genome-wide expression profiles. *Proc Natl Acad Sci USA*. 2005;102(43):15545-15550.
- Scott DW, Wright GW, Williams PM, et al. Determining cell-of-origin subtypes of diffuse large B-cell lymphoma using gene expression in formalin-fixed paraffin-embedded tissue. *Blood*. 2014;123(8):1214-1217.
- Brastianos PK, Horowitz PM, Santagata S, et al. Genomic sequencing of meningiomas identifies oncogenic SMO and AKT1 mutations. *Nat Genet*. 2013;45(3):285-289.
- Li H, Durbin R. Fast and accurate short read alignment with Burrows-Wheeler transform. *Bioinformatics*. 2009;25(14):1754-1760.
- McKenna A, Hanna M, Banks E, et al. The Genome Analysis Toolkit: a MapReduce framework for analyzing next-generation DNA sequencing data. *Genome Res*. 2010;20(9):1297-1303.
- DePristo MA, Banks E, Poplin R, et al. A framework for variation discovery and genotyping using next-generation DNA sequencing data. *Nat Genet*. 2011;43(5):491-498.
- Cibulskis K, Lawrence MS, Carter SL, et al. Sensitive detection of somatic point mutations in impure and heterogeneous cancer samples. *Nat Biotechnol*. 2013;31(3):213-219.
- Abo RP, Ducar M, Garcia EP, et al. BreakM: detection of structural variation in targeted massively parallel sequencing data using kmers. *Nucleic Acids Res*. 2015;43(3):e19.
- McLaren W, Pritchard B, Rios D, Chen Y, Flicek P, Cunningham F. Deriving the consequences of genomic variants with the Ensembl API and SNP Effect Predictor. *Bioinformatics*. 2010;26(16):2069-2070.
- Langerak AW, Groenen PJ, Brüggemann M, et al. EuroClonality/BIOMED-2 guidelines for interpretation and reporting of Ig/TCR clonality testing in suspected lymphoproliferations. *Leukemia*. 2012;26(10):2159-2171.
- Swerdlow SH, Campo E, Harris NL, et al, eds. WHO Classification of Tumours of Haematopoietic and Lymphoid Tissues. 4th ed. Lyon, France: IARC Press; 2008.
- Polo JM, Juszczynski P, Monti S, et al. Transcriptional signature with differential expression of BCL6 target genes accurately identifies BCL6-dependent diffuse large B cell lymphomas. *Proc Natl Acad Sci USA*. 2007;104(9):3207-3212.
- Weiss LM, Warnke RA, Sklar J, Cleary ML. Molecular analysis of the t(14;18) chromosomal translocation in malignant lymphomas. *N Engl J Med*. 1987;317(19):1185-1189.

49. Yoon SO, Jeon YK, Paik JH, et al. MYC translocation and an increased copy number predict poor prognosis in adult diffuse large B-cell lymphoma (DLBCL), especially in germinal centre-like B cell (GCB) type. *Histopathology*. 2008;53(2):205-217.
50. Horn H, Ziepert M, Becher C, et al; German High-Grade Non-Hodgkin Lymphoma Study Group. MYC status in concert with BCL2 and BCL6 expression predicts outcome in diffuse large B-cell lymphoma. *Blood*. 2013;121(12):2253-2263.
51. Visco C, Tzankov A, Xu-Monette ZY, et al. Patients with diffuse large B-cell lymphoma of germinal center origin with BCL2 translocations have poor outcome, irrespective of MYC status: a report from an International DLBCL rituximab-CHOP Consortium Program Study. *Haematologica*. 2013;98(2):255-263.
52. Barrans SL, Evans PA, O'Connor SJ, et al. The t(14;18) is associated with germinal center-derived diffuse large B-cell lymphoma and is a strong predictor of outcome. *Clin Cancer Res*. 2003;9(6):2133-2139.
53. Iqbal J, Sanger WG, Horsman DE, et al. BCL2 translocation defines a unique tumor subset within the germinal center B-cell-like diffuse large B-cell lymphoma. *Am J Pathol*. 2004;165(1):159-166.
54. Pasqualucci L, Dominguez-Sola D, Chiarenza A, et al. Inactivating mutations of acetyltransferase genes in B-cell lymphoma. *Nature*. 2011;471(7337):189-195.
55. Morin RD, Mungall K, Pleasance E, et al. Mutational and structural analysis of diffuse large B-cell lymphoma using whole-genome sequencing. *Blood*. 2013;122(7):1256-1265.
56. Currie KS, Kropf JE, Lee T, et al. Discovery of GS-9973, a selective and orally efficacious inhibitor of spleen tyrosine kinase. *J Med Chem*. 2014;57(9):3856-3873.
57. Sharman J, Hawkins M, Kolibaba K, et al. An open-label phase 2 trial of entospletinib (GS-9973), a selective spleen tyrosine kinase inhibitor, in chronic lymphocytic leukemia. *Blood*. 2015;125(15):2336-2343.
58. Burke RT, Meadows S, Loriaux MM, et al. A potential therapeutic strategy for chronic lymphocytic leukemia by combining Idelalisib and GS-9973, a novel spleen tyrosine kinase (Syk) inhibitor. *Oncotarget*. 2014;5(4):908-915.
59. Lenz G, Wright G, Dave SS, et al; Lymphoma/Leukemia Molecular Profiling Project. Stromal gene signatures in large-B-cell lymphomas. *N Engl J Med*. 2008;359(22):2313-2323.
60. DeRose YS, Wang G, Lin YC, et al. Tumor grafts derived from women with breast cancer authentically reflect tumor pathology, growth, metastasis and disease outcomes. *Nat Med*. 2011;17(11):1514-1520.
61. Béguelin W, Popovic R, Teater M, et al. EZH2 is required for germinal center formation and somatic EZH2 mutations promote lymphoid transformation. *Cancer Cell*. 2013;23(5):677-692.
62. Bernal F, Wade M, Godes M, et al. A stapled p53 helix overcomes HDMX-mediated suppression of p53. *Cancer Cell*. 2010;18(5):411-422.
63. Chang YS, Graves B, Guerlavais V, et al. Stapled  $\alpha$ -helical peptide drug development: a potent dual inhibitor of MDM2 and MDMX for p53-dependent cancer therapy. *Proc Natl Acad Sci USA*. 2013;110(36):E3445-E3454.





2016 127: 2203-2213

doi:10.1182/blood-2015-09-672352 originally published  
online January 15, 2016

## **Diffuse large B-cell lymphoma patient-derived xenograft models capture the molecular and biological heterogeneity of the disease**

Bjoern Chapuy, Hongwei Cheng, Akira Watahiki, Matthew D. Ducar, Yuxiang Tan, Linfeng Chen, Margaretha G. M. Roemer, Jing Ouyang, Amanda L. Christie, Liye Zhang, Daniel Gusenleitner, Ryan P. Abo, Pedro Farinha, Frederike von Bonin, Aaron R. Thorner, Heather H. Sun, Randy D. Gascoyne, Geraldine S. Pinkus, Paul van Hummelen, Gerald G. Wulf, Jon C. Aster, David M. Weinstock, Stefano Monti, Scott J. Rodig, Yuzhuo Wang and Margaret A. Shipp

---

Updated information and services can be found at:

<http://www.bloodjournal.org/content/127/18/2203.full.html>

Articles on similar topics can be found in the following Blood collections

[Lymphoid Neoplasia](#) (2488 articles)

---

Information about reproducing this article in parts or in its entirety may be found online at:

[http://www.bloodjournal.org/site/misc/rights.xhtml#repub\\_requests](http://www.bloodjournal.org/site/misc/rights.xhtml#repub_requests)

Information about ordering reprints may be found online at:

<http://www.bloodjournal.org/site/misc/rights.xhtml#reprints>

Information about subscriptions and ASH membership may be found online at:

<http://www.bloodjournal.org/site/subscriptions/index.xhtml>